Effects of finite-size neutrally buoyant particles on the turbulent flows in a square duct

Zhaowu Lin, Zhaosheng Yu, Xueming Shao, and Lian-Ping Wang

Citation: Physics of Fluids **29**, 103304 (2017); doi: 10.1063/1.5002663
View online: http://dx.doi.org/10.1063/1.5002663
View Table of Contents: http://aip.scitation.org/toc/phf/29/10
Published by the American Institute of Physics

Effects of finite-size neutrally buoyant particles on the turbulent flows in a square duct

Zhaowu Lin,[1] Zhaosheng Yu,[1,a)] Xueming Shao,[1] and Lian-Ping Wang[2]
[1]*State Key Laboratory of Fluid Power and Mechatronic Systems, Department of Mechanics, Zhejiang University, Hangzhou 310027, China*
[2]*Department of Mechanical Engineering, University of Delaware, Newark, Delaware 19716, USA*

(Received 31 August 2017; accepted 28 September 2017; published online 16 October 2017)

Interface-resolved direct numerical simulations of the particle-laden turbulent flows in a square duct are performed with a direct-forcing fictitious domain method. The effects of the finite-size particles on the mean and root-mean-square (RMS) velocities are investigated at the friction Reynolds number of 150 (based on the friction velocity and half duct width) and the particle volume fractions ranging from 0.78% to 7.07%. Our results show that the mean secondary flow is enhanced and its circulation center shifts closer to the center of the duct cross section when the particles are added. The reason for the particle effect on the mean secondary flow is analyzed by examining the terms in the mean streamwise vorticity equation. It is observed that the particles enhance the gradients of the secondary Reynolds normal stress difference and shear stress in the near-wall region near the corners, which we think is mainly responsible for the enhancement in the mean secondary flow. Under a prescribed driving pressure gradient, the presence of particles attenuates the bulk velocity and the turbulent intensity. All particle-induced effects are intensified with increasing particle volume fraction and decreasing particle size, if other parameters are fixed. In addition, the particles accumulate preferentially in the near-corner region. The effects of the type of the collision model (i.e., if friction and damping are included or not) on the results are found significant, but not so significant to bring about qualitatively different results. *Published by AIP Publishing.* https://doi.org/10.1063/1.5002663

I. INTRODUCTION

The turbulent flow in a square duct is characterized by the presence of mean cross-stream fluid motions, classified as the secondary flow of Prandtl' second kind.[1] This kind of secondary flows, induced by turbulence fluctuations, takes the form of eight symmetrical vortices, with two counter-rotating vortices in pairs in each quadrant of the duct. The mean secondary flows transport the fluid momentum from the bulk region to the corner areas along each corner bisector and then back to the bulk regions along the wall bisectors. The mean secondary flow in a square duct was first recognized by Prandtl[1] from the experiments of Nikuradse.[2] Further experimental measurements of the turbulent flows in a square duct were conducted by Brundrett and Baines,[3] Gessner,[4] and Melling and Whitelaw,[5] with the focus on the Reynolds stresses as the source for the generation of mean secondary flows. Direct numerical simulations of the turbulent flow in a square duct have been performed by Gavrilakis,[6] Huser and Biringen,[7] Uhlmann *et al.*,[8] and Pinelli *et al.*[9] Gavrilakis[6] examined the statistics of the turbulence and the budget for the mean streamwise vorticity and observed that viscous effects were much greater than the mean convection. Huser and Biringen[7] demonstrated that the mean secondary flow pattern and the anisotropic Reynolds stress distribution could be explained by the preferred location of an ejection structure near the corner and the interaction between bursts from the two intersecting walls. Uhlmann *et al.*[8] observed that at marginal (low) Reynolds numbers, the short-time-averaged velocity fields exhibited a four-vortex state characterized by two pairs of counter-rotating vortices associated with a pair of opposite walls, and long-time-averaged velocity fields exhibited a common eight-vortex pattern. Pinelli *et al.*[9] focused on dynamical mechanisms for the behaviour of mean velocity values when increasing the Reynolds number: the deformation of the mean streamwise velocity and the shape of mean secondary flow, and argued that mean streamwise vorticity strongly depended upon statistically preferred location of the quasi-streamwise vortices associated with the pair of fast/slow streaks closest to the corner.

There are limited studies on the particle-laden turbulent flows in a square duct in the literature. Winkler *et al.*[10] investigated the preferential concentration of particles in a fully developed turbulent square duct flow and observed that particles tended to accumulate in regions of high strain-rate and low swirling strength. Sharma and Phares[11] reported that the mean secondary flow enhanced the lateral mixing for passive tracers and low-inertia particles, and higher inertia particles accumulated close to the wall. Winkler *et al.*,[12] Yao and Fairweather,[13] and Yao *et al.*[14] investigated the particle deposition in turbulent square duct flows. The results of Winkler *et al.*[12] showed that the deposition occurred with greater probability near the center of the duct walls than at the corners, whereas Yao and Fairweather[13] and Yao *et al.*[14] concluded that high-inertia particles tended to deposit close to the

a)Author to whom correspondence should be addressed: yuzhaosheng@zju.edu.cn

corners of the duct floor, while low-inertia particles deposited near the floor center. Yao and Fairweather[15] investigated the resuspension of inertial particles in a turbulent square duct flow and demonstrated the important role of the mean secondary flow in the resuspension process.

For all studies on the two-phase flows above, the point-particle approximation was employed to deal with the particle motion, which is valid in principle only when the particle size is smaller than the Kolmogorov length scale and the particle volume fraction is low. In recent years, the interface-resolved direct numerical simulation methods have been used to probe the mechanisms in the interactions between the turbulence and the finite-size particles, in which the interface between the particles and fluids is resolved and all turbulent structures are resolved with the direct numerical simulation method. Such methods have been applied to the simulations of particle-laden isotropic homogeneous flows (e.g., Ten Cate *et al.*,[16] Lucci *et al.*,[17] Gao *et al.*,[18] and Cisse *et al.*[19]), pipe flow,[20] vertical channel flows,[21,22] and horizontal channel flows (e.g., Pan and Banerjee,[23] Shao *et al.*,[24] Kidanemariam *et al.*,[25] Do-Quang *et al.*,[26] Picano *et al.*,[27] Wang *et al.*[28]), as well as the interactions between the turbulence and a fixed particle (e.g., Bagchi and Balachandar,[29] Burton and Eaton,[30] Naso and Prosperetti[31]). The aim of the present work is to investigate the effects of the finite-size neutrally buoyant particles on the turbulent flows in a square duct with the interface-resolved DNS method, focusing on the mean and root-mean-square velocities and in particular the mean secondary flow. We note that a companion paper on the effects of the heavy particles on the turbulent duct flow has recently been published during the revision of the present work.[32]

The paper is organized as follows. In Sec. II, we describe our numerical model and method. The accuracy of our computations is first validated for the case of single-phase flows in Sec. III. In Sec. IV, our results on the mean secondary flow, the mean streamwise velocity, the RMS velocities, and the solid-phase statistics (mainly on the distribution of the particle concentration) are presented and discussed. Concluding remarks are presented in Sec. V.

II. NUMERICAL MODEL

A. Flow model

A schematic diagram of the geometrical model for the duct flow studied is shown in Fig. 1. The x-axis is aligned with the streamwise direction. For the neutrally buoyant case considered, the y-axis and z-axis are exchangeable. For convenience, we refer to the z-axis-direction as the spanwise direction, as for the plane channel flow case. The corresponding velocity components in the (x, y, z) direction are $\mathbf{u} = (u, v, w)$, respectively. The no-slip velocity boundary condition is imposed at the duct walls and the periodic boundary condition is imposed in the streamwise direction. We denote the half width of the duct as H. In the present study, the computational domain is $[0, 16H] \times [-H, H] \times [-H, H]$.

We take H as the characteristic length and the friction velocity u_τ as the characteristic velocity to non-dimensionalize physical quantities. The friction velocity is defined as $u_\tau = \sqrt{\tau_w/\rho_f}$, here τ_w being the mean shear stress of the suspension on the walls, and ρ_f is the fluid density. Thus, the Reynolds number is defined by $Re_\tau = u_\tau H/\nu$, ν being the fluid kinematic viscosity. The pressure gradient is kept constant in our simulations, being $(-dp/dx)^e = 2\tau_w/H$, and its dimensionless value normalized by $\rho_f u_\tau^2/H$ is 2.

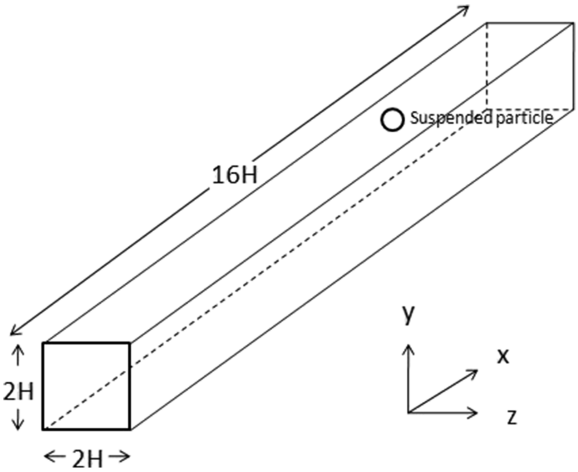

FIG. 1. Geometrical model for the duct flow.

B. Direct-forcing fictitious domain method

A parallel direct-forcing fictitious domain method (DF/FD) is employed for the simulation of particle-laden turbulent duct flows.[33] The fictitious domain (FD) method for the particulate flows was originally proposed by Glowinski *et al.*[34] The key idea of this method is that the interior of each particle is filled with the fluid and the inner fictitious fluid is enforced to satisfy the rigid body motion constraint through a pseudo body force, which is introduced as a distributed Lagrange multiplier in the FD formulation.[34] In the following, we describe the DF/FD method briefly, and the reader is referred to the work of Yu and Shao[35] for further details.

For simplicity of description, we will consider only one spherical particle in the following exposition. The particle density, volume and moment of inertia, translational velocity, angular velocity, and position are denoted by ρ_s, V_p, J, $\mathbf{U}$, $\boldsymbol{\omega}_p$, and $\mathbf{X}_p$, respectively. Let $P(t)$ represent the solid domain and Ω represent the entire domain including the interior and exterior of the solid body. By introducing the following scales for the purpose of non-dimensionalization: H for the length, u_τ for the velocity, H/u_τ for the time, $\rho_f u_\tau^2$ for the pressure, and $\rho\ \rho_f u_\tau^2/H$ for the pseudo body force, the dimensionless FD formulation for the incompressible fluids and the spherical particles can be written as follows:

$$\frac{\partial \mathbf{u}}{\partial t} + \mathbf{u}\cdot\nabla\mathbf{u} = \frac{\nabla^2\mathbf{u}}{Re_\tau} - \nabla p + 2\boldsymbol{e}_x + \boldsymbol{\lambda} \quad \text{in } \Omega, \tag{1}$$

$$\mathbf{u} = \mathbf{U} + \boldsymbol{\omega}_p \times \mathbf{r} \quad \text{in } P(t), \tag{2}$$

$$\nabla\cdot\mathbf{u} = 0 \quad \text{in } \Omega, \tag{3}$$

$$(\rho_r - 1)V_p^*\left(\frac{\mathrm{d}\mathbf{U}}{\mathrm{d}t} - Fr\frac{\mathbf{g}}{g}\right) = -\int_P \boldsymbol{\lambda}\,\mathrm{d}\mathbf{x}, \tag{4}$$

$$(\rho_r - 1)J^*\frac{\mathrm{d}\boldsymbol{\omega}_p}{\mathrm{d}t} = -\int_P \mathbf{r}\times\boldsymbol{\lambda}\,\mathrm{d}\mathbf{x}. \tag{5}$$

In the above equations, $\mathbf{u}$ represents the fluid velocity, p represents the local fluid pressure with the exclusion of the constant pressure gradient of $2\boldsymbol{e}_x$ ($\boldsymbol{e}_x$ being the unit vector pointing to the streamwise direction), $\boldsymbol{\lambda}$ represents the pseudo-body force that is non-zero only in the solid domain $P(t)$, $\mathbf{r}$ represents the position vector with respect to the mass center of the particle, ρ_r represents the particle-fluid density ratio defined by $\rho_r = \rho_s/\rho_f$, Fr represents the Froude number defined here by $Fr = gH/u_\tau^2$, V_p^* represents the dimensionless particle volume define by $V_p^* = V_p/H^3$, and J^* represents the dimensionless moment of inertia defined by $J^* = J/\rho_s H^5$.

A fractional-step time integration scheme is used to decouple system (1)–(5) into the following two sub-problems.

Fluid sub-problem for $\mathbf{u}^*$ and p,

$$\frac{\mathbf{u}^* - \mathbf{u}^n}{\Delta t} - \frac{1}{2}\frac{\nabla^2 \mathbf{u}^*}{Re_\tau} = -\nabla p + 2\boldsymbol{e}_x - \frac{1}{2}\left[3(\mathbf{u}\cdot\nabla\mathbf{u})^n - (\mathbf{u}\cdot\nabla\mathbf{u})^{n-1}\right] + \frac{1}{2}\frac{\nabla^2 \mathbf{u}}{Re_\tau} + \boldsymbol{\lambda}^n, \tag{6}$$

$$\nabla\cdot\mathbf{u}^* = 0. \tag{7}$$

A finite-difference-based projection method on a homogeneous half-staggered grid is used for the solution of the above fluid sub-problem. The grid is homogeneous in all three directions. For the half-staggered scheme, the pressure is defined at the cell center and all velocity components are defined on the grid nodes. All spatial derivatives are discretized with the second-order central difference scheme.

Particle sub-problem for $\mathbf{U}^{n+1}, \omega_p^{n+1}, \boldsymbol{\lambda}^{n+1}$, and $\mathbf{u}^{n+1}$,

$$\rho_r V_p^* \frac{\mathbf{U}^{n+1}}{\Delta t} = \left(\rho_r - 1\right) V_p^* \left(\frac{\mathbf{U}^n}{\Delta t} - Fr\frac{\mathbf{g}}{g}\right) + \int_P \left(\frac{\mathbf{u}^*}{\Delta t} - \boldsymbol{\lambda}^n\right) \mathrm{d}\,\mathbf{x}, \tag{8}$$

$$\rho_r \frac{J^* \omega_p^{n+1}}{\Delta t} = (\rho_r - 1)\frac{J^* \omega_p^n}{\Delta t} + \int_P r \times \left(\frac{\mathbf{u}^*}{\Delta t} - \boldsymbol{\lambda}^n\right) d\mathbf{x}. \tag{9}$$

Note that the above equations have been reformulated so that all the right-hand side terms are known quantities and consequently the particle velocities $\mathbf{U}^{n+1}$ and $\boldsymbol{\omega}_p^{n+1}$ are obtained without iteration. Then, $\boldsymbol{\lambda}^{n+1}$ defined at the Lagrangian nodes are determined from

$$\boldsymbol{\lambda}^{n+1} = \frac{\mathbf{U}^{n+1} + \boldsymbol{\omega}_p^{n+1}\times\mathbf{r} - \mathbf{u}^*}{\Delta t} + \boldsymbol{\lambda}^n. \tag{10}$$

Finally, the fluid velocities $\mathbf{u}^{n+1}$ at the Eulerian nodes are corrected from

$$\mathbf{u}^{n+1} = \mathbf{u}^* + \Delta t\left(\boldsymbol{\lambda}^{n+1} - \boldsymbol{\lambda}^n\right). \tag{11}$$

In the above manipulations, the tri-linear function is used to transfer the fluid velocity from the Eulerian nodes to the Lagrangian nodes, and the pseudo body force from the Lagrangian nodes to the Eulerian nodes.

C. Particle-particle and particle-wall collision model

The collision model is required to prevent the mutual penetration of particles and the penetration of particles into walls. Two soft-sphere collision models are adopted in the present study, in order to examine the effects of the collision model on the results. One is the following Artificial Repulsive Force (referred to as ARF) collision model:

$$\mathbf{F} = F_0(1 - d/d_c)\mathbf{n}, \tag{12}$$

where $\mathbf{F}$, d, and $\mathbf{n}$ are the repulsive force, the gap distance, and the unit normal vector between the particles i and j, respectively. d_c represents a cutoff distance and the repulsive force is activated when $d < d_c$. F_0 is the magnitude of the force at contact. We set $d_c = h$ (h being the fluid mesh size) and $F_0 = 10^3$. The motions of the particles due to the collision force (12) and due to the hydrodynamic force (8) and (9) are handled separately with a fractional step scheme. The time step for the collision interactions is set to be one tenth of the latter (i.e., $\Delta t/10$) to circumvent the stiffness problem rising from the explicit integration scheme with a large value of F_0, as suggested by Glowinski *et al.*[34] The collision between a particle and a wall is treated similarly as two particles with the coefficient F_0 in (12) doubled. This collision model was used by Shao *et al.*[24] to study particle-laden turbulent channel flows.

The other collision model adopted is the Discrete Element Model (referred to as DEM) developed originally for the simulation of granular materials. The DEM collision model uses the mechanical elements such as a spring and a dash-dot. Besides the spring-like repulsive force, the viscous damping force in the normal direction and the tangential (friction) force are also considered. We adopt the model described by Crowe *et al.*,[36]

$$\mathbf{F}_n = (-k_n\delta_n^{3/2} - \eta_n\mathbf{G}\cdot\mathbf{n})\mathbf{n}, \tag{13}$$

$$\mathbf{F}_t = -k_t\boldsymbol{\delta}_t - \eta_t\mathbf{G}_{ct}, \tag{14}$$

where $\mathbf{F}_n$, δ_n, k_n, and η_n are the contact force on particle i, overlap distance, spring coefficient, and damping coefficient in the normal direction, respectively, and $\mathbf{F}_t$, $\boldsymbol{\delta}_t$, k_t, and η_t are the corresponding parameters in the tangential direction. Here $\mathbf{n}$ is the unit vector in the direction of the line from the center of particle i to that of particle j, and $\mathbf{G}$ is the velocity vector of particle i relative to particle j ($\mathbf{G} = \mathbf{U}_i - \mathbf{U}_j$). $\mathbf{G}_{ct}$ is the slip velocity given by

$$\mathbf{G}_{ct} = \mathbf{G} - (\mathbf{G}\cdot\mathbf{n})\mathbf{n} + a_i\boldsymbol{\omega}_{pi}\times\mathbf{n} + a_j\boldsymbol{\omega}_{pj}\times\mathbf{n}, \tag{15}$$

If the following relation is satisfied

$$|\mathbf{F}_t| > f|\mathbf{F}_n|, \tag{16}$$

particle i slides and the tangential force is given by the Coulomb-type friction law

$$\mathbf{F}_t = -f|\mathbf{F}_n|\mathbf{t}, \tag{17}$$

where f is the friction coefficient and $\mathbf{t}$ is the unit vector of $\mathbf{G}_{ct}$. In this study, we set friction coefficient $f = 0.3$ for particles interacting with other particles and $f = 0.2$ with the walls.

The stiffness k_n of a sphere is expressed using the Hertzian contact theory

$$k_n = \frac{4}{3}\left(\frac{1-\sigma_i^2}{E_i} + \frac{1-\sigma_j^2}{E_j}\right)^{-1}\left(\frac{a_i + a_j}{a_i a_j}\right)^{-1/2}, \tag{18}$$

where E and σ are Young's modulus and the Poisson ratio, respectively. The stiffness k_t can be given using Mindlin's theory

$$k_t = 8\left(\frac{2-\sigma_i}{G_i} + \frac{2-\sigma_j}{G_j}\right)^{-1}\left(\frac{a_i + a_j}{a_i a_j}\right)^{-1/2}\delta_n^{1/2}, \tag{19}$$

where G is the particle shear modulus, which is related to Young's modulus and the Poisson ratio, as follows:

$$G = \frac{E}{2(1+\sigma)}. \tag{20}$$

Damping coefficients are given by

$$\eta_n = 2\sqrt{m_p k_n},\ \eta_t = 2\sqrt{m_p k_t}, \tag{21}$$

where m_p is the mass of particle. In our work, we set $E = 3 \times 10^5$ and $\sigma = 0.33$. The time step for the DEM collision model is also set to be one tenth of that for the fluid fields (i.e., $\Delta t/10$), as in the ARF model. As pointed out by Crowe *et al.*,[36] the elastic modulus adopted in the DEM simulation is normally less than the real value to avoid the excessively small time step, and the results are not sensitive to the choice of the value, particularly for the particle collision in fluids.

The ARF model can be taken as an extreme case of the DEM model where the coefficients for the friction and damping forces are zero, and therefore the difference in the results obtained by two types of collision model reflects the effects of the collision model for the extreme case. It is beyond the scope of the present study to examine in detail the effects of the parameters in the collision model. Unless otherwise specified, the results reported below are obtained with the ARF collision model. We note that Kempe and Fröhlich[37] proposed a sophisticated collision model for the interface-resolved simulations of particle-laden flows.

D. Parameter settings

The friction Reynolds number Re_τ is 150, throughout this study. Two particle sizes are considered: $a/H = 0.05$ and 0.1, here a being the particle radius. The particle volume fractions are $\phi = 0.78\%$, 2.36%, and 7.07%. The Froude number (Fr) is zero since only the neutrally buoyant case is considered.

The grid number for our computations is $1024 \times 128 \times 128$, corresponding to the mesh size $h = H/64$. The time step is $0.0002\ H/u_\tau$. The flow statistics are obtained from averaging the data in the real fluid domain outside the particle boundaries over a period of typically 50 non-dimensional time units after the statistically stationary state is reached.

III. VALIDATION

Due to lack of data on the duct flow laden with finite-size particles, we compare our results for the single-phase case to the previous direct numerical simulations of Gavrilakis[6] and Pinelli *et al.*[9] to validate the accuracy of our computations. Gavrilakis[6] adopted a constant pressure gradient at $Re_\tau = 150$ and a larger streamwise domain of $L_x = 20\pi H$, while Pinelli *et al.*[9] kept the flow flux constant at $Re_b = U_b H/\nu = 2205$, corresponding to $Re_\tau \approx 150$. Here U_b denotes the bulk velocity. The mean streamwise and spanwise velocity profiles at $z = -0.7$ and the root-mean-square (RMS) values of the streamwise and spanwise fluctuating velocities at $z = -0.3$ are presented in Figs. 2 and 3, respectively. The velocities are normalized by the bulk velocity U_b. A good agreement is found between our results and the reference data. Our streamwise RMS velocity is slightly larger than those of Gavrilakis[6] and Pinelli *et al.*[9] The reason is not clear. Our streamwise RMS velocity for $L_x = 8H$ was observed to be higher than that for $L_x = 16H$, which indicates that the effect of the streamwise domain size might be one reason for the discrepancy between our results and those of Gavrilakis.[6] This is also the reason why we chose $L_x = 16H$ for our simulations. Further increases in the streamwise domain size and the grid resolution are limited by our use of the homogeneous mesh with the grid number of 2^N (N being an integer) in each direction and our computational resource.

For the particle-laden case of $a/H = 0.05$, there are only 3.2 meshes per particle radius, and one may question whether such mesh resolution is high enough to ensure acceptable accuracy. It was demonstrated in our previous study[24] that

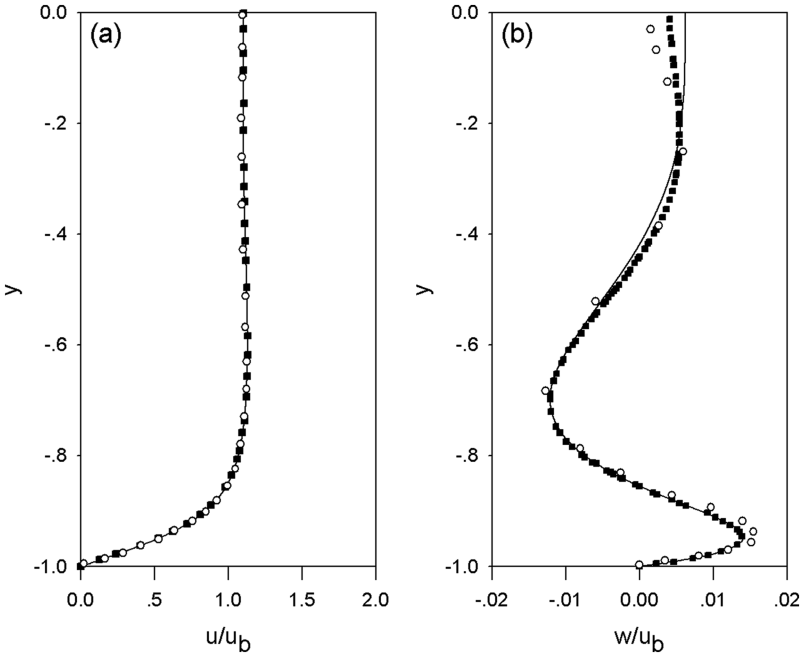

FIG. 2. Mean velocity profiles at $z = -0.7$ for the single-phase duct flow normalized by the bulk velocity at $Re_\tau = 150$: (a) streamwise component and (b) spanwise component. Present results (solid lines), Gavrilakis[6] (○) and Pinelli *et al.*[9] (■).

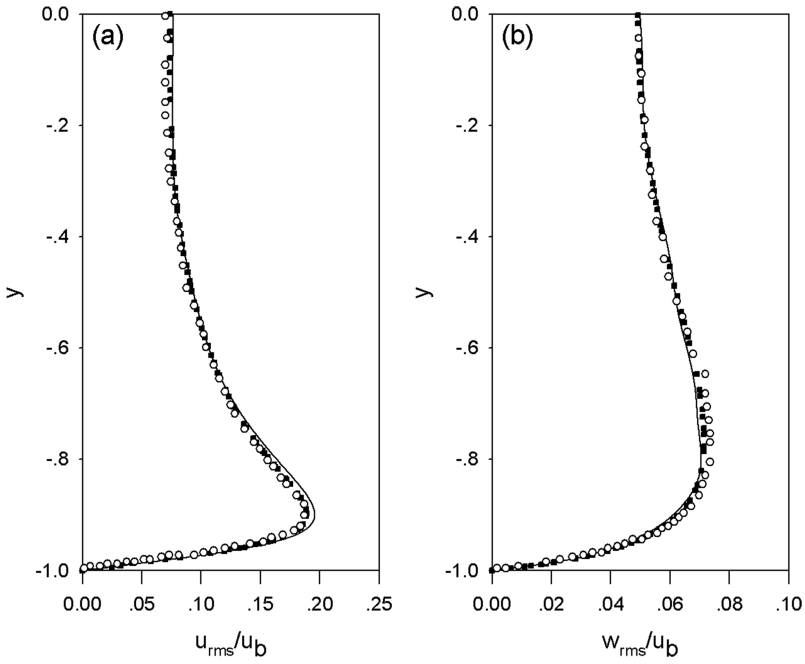

FIG. 3. Profiles of the root-mean-square values of the velocity fluctuations at $z = -0.3$ for the single-phase duct flow normalized by the bulk velocity at $Re_\tau = 150$: (a) streamwise component and (b) spanwise component. Present results (solid lines), Gavrilakis[6] (○) and Pinelli *et al.*[9] (■).

the drag coefficient for a spherical particle settling in a wide channel obtained using our FD method with $h = a/3.2$ was reasonably accurate for the particle Reynolds number up to 50. For the present study, we do not have sufficient computer resources to perform a mesh-convergence test. Nevertheless, we conducted a mesh convergence test for a particle-laden turbulent channel flow at $Re_\tau = 180$, $\phi = 0.84\%$, and $\rho_r = 104.2$ in our previous study[33] and observed that the results obtained with $h = a/3.2$ and $h = a/6.4$ are in good agreement with each other. This mesh-convergence test may not necessarily guarantee that the present results on the secondary flow for $h = a/3.2$ (i.e., $a/H = 0.05$) are accurate. However, our results for $a/H = 0.1$ (with $h = a/6.4$) should be more reliable, and this is the reason why we analyze the particle effect on the secondary flow primarily with data for $a/H = 0.1$. We will see that the results for $h = a/3.2$ and $h = a/6.4$ are qualitatively the same.

IV. RESULTS AND DISCUSSION

We will present and discuss our results on the mean secondary flow, the mean streamwise velocity, the RMS velocities, and the solid-phase statistics in Subsections IV A–IV D.

A. Mean secondary flow

Figures 4(a) and 4(b) show the velocity vectors of the mean secondary flow for the single-phase case and the particle-laden case at $a/H = 0.1$ and $\phi = 7.07\%$ in a quadrant of the domain, respectively. Note that all flow statistics are computed with the data in the real fluid domain outside the particles. The mean flow takes the form of a pair of counter-rotating vortices in each quadrant, transporting the fluid momentum from the bulk region to the corner along the corner bisector. By comparing Figs. 4(a) and 4(b), it is observed that the positions of the vortex centers for the particle-laden case shift further away from the walls nearby (i.e., closer to the cross-section centerlines) in both the y and z directions, compared to the single-phase case. To illustrate the effect of the particles on the intensity of the mean secondary flow, we compute the mean secondary-flow stream-function from the mean streamwise vorticity $\bar{\omega}_x$,

$$\nabla^2 \bar{\psi} = -\bar{\omega}_x. \tag{22}$$

The contours of the stream-functions $\bar{\psi}(y, z)$ for the particle-free flow and the particle-laden flow at $a/H = 0.05$ and $\phi = 7.07\%$ are plotted in Figs. 4(c) and 4(d), respectively. The maximum of the stream-function reflects the flow rate (flux) in the circulation. Clearly the addition of the particles enhances the mean secondary flow. Note that the increment for all contours in comparison is the same, throughout this paper.

The positions of the centers and the maxima of the stream-functions of the mean secondary flows in the lower octant in Fig. 4 for different particle sizes and volume fractions are plotted in Figs. 5(a) and 5(b), respectively. The results indicate that the circulation centers shift closer to the cross-section center and the mean secondary flow is intensified, as the particle volume fraction increases at the same particle size, or the particle radius decreases at the same volume fraction. The relative change in the center position in the z-axis direction is generally more significant than in the y-axis direction for the vortex in the lower octant, presumably due to tighter constraint of the symmetry from the corner bisector than the wall bisector (i.e., cross-section centerline).

To show the effects of the particle collision model, both results obtained from the ARF and DEM models are plotted in Fig. 5. The mean secondary flows with the DEM model are generally weaker compared to those with the ARF model but still stronger than that for the particle-free case.

We now attempt to explain why the particle addition enhances the mean secondary flow. The governing equation for the mean streamwise vorticity was used to analyze the mechanism for the generation of the mean secondary flow in

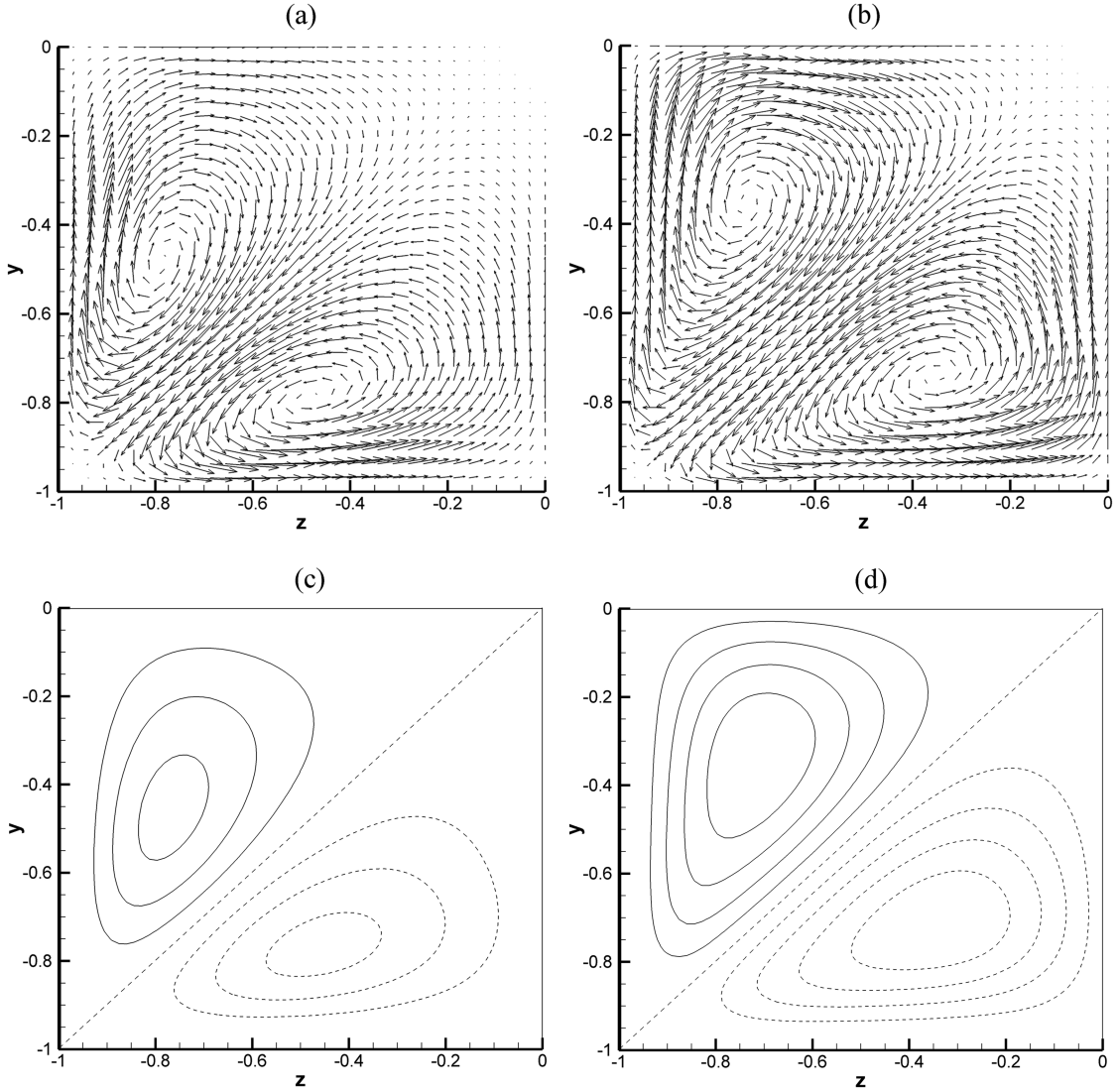

FIG. 4. Mean secondary velocity vectors for (a) particle-free flow, (b) particle-laden flow at $a/H = 0.1$ and $\phi = 7.07\%$, and contours of stream-functions $\bar{\psi}(y, z)$ for (c) particle-free flow and (d) particle-laden flow at $a/H = 0.05$ and $\phi = 7.07\%$. Only a quadrant of the domain is shown. The increment for the stream-function contours is 0.01.

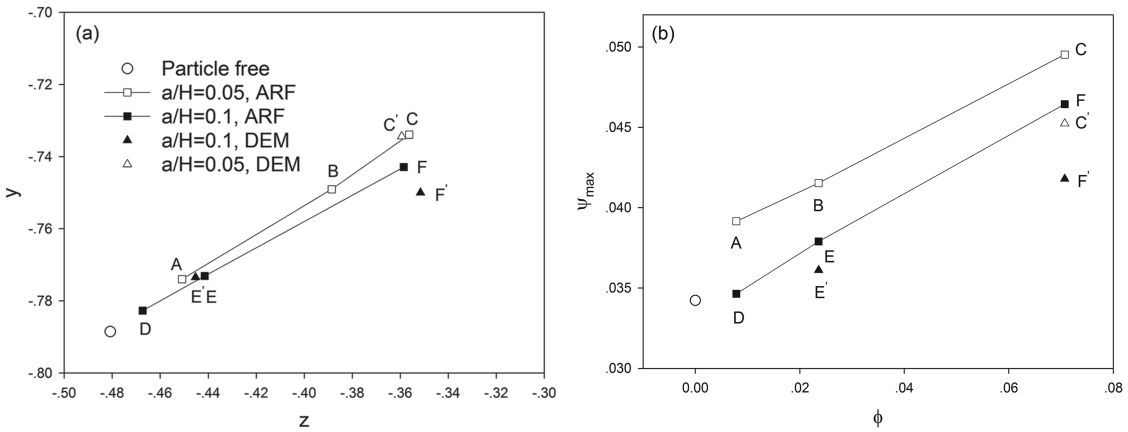

FIG. 5. (a) Positions of the centers and (b) maxima of the stream functions of the mean secondary flows. Point "A": $a/H = 0.05$, $\phi = 0.78\%$; "B": $a/H = 0.05$, $\phi = 2.36\%$; "C": $a/H = 0.05$, $\phi = 7.07\%$; "D": $a/H = 0.1$, $\phi = 0.78\%$; "E": $a/H = 0.1$, $\phi = 2.36\%$; "F": $a/H = 0.1$, $\phi = 7.07\%$; "C′": $a/H = 0.05$, $\phi = 7.07\%$ (with DEM); "E′": $a/H = 0.1$, $\phi = 2.36\%$ (with DEM); "F′": $a/H = 0.1$, $\phi = 7.07\%$ (with DEM).

the single-phase case (e.g., Brundrett and Baines;[3] Perkins[38]), which has a simple form for a fully developed flow,

$$\underbrace{\left(\overline{v}\frac{\partial\overline{\omega_x}}{\partial y}+\overline{w}\frac{\partial\overline{\omega_x}}{\partial z}\right)}_{\text{Convection term}}+\underbrace{\left(\frac{\partial^2}{\partial y\partial z}(\overline{w'^2}-\overline{v'^2})\right)}_{\text{Normall stress term}}+\underbrace{\left((\frac{\partial^2}{\partial y^2}-\frac{\partial^2}{\partial z^2})\overline{v'w'}\right)}_{\text{Shear stress term}}+\underbrace{\left(-\frac{1}{Re_\tau}(\frac{\partial^2}{\partial y^2}+\frac{\partial^2}{\partial z^2})\overline{\omega_x}\right)}_{\text{Viscous diffusion term}}=0. \quad (23)$$

The terms in the first bracket on the left-hand side of (23) represent the convection of the mean vorticity by the secondary flow itself. The last term represents the viscous diffusion of the mean vorticity. The other two terms are related to the Reynolds stresses arising from the Reynolds averaging of the Navier-Stokes equation, generally described as the source of vorticity.[6] The first term is associated with the gradients in the Reynolds cross-stream normal stress difference, and the second term is associated with the Reynolds secondary shear stress.

The flow statistics in Eq. (23) for the particle-laden case in our simulations are calculated with the data in the real fluid domain. The average values of the velocities and the Reynolds stress shear are first calculated on the Eulerian grids (the data on the Eulerian grids inside the particle boundaries are discarded for averaging) and their derivatives are then computed mainly with the central difference scheme. For each time level, if all data for the calculation of the derivatives are defined on the grids in the fluid domain and used for the averaging, then Eq. (23) theoretically holds since the averaging and differential manipulations can be commuted, as in the particle-free case. However, for the particle-laden case, the data on the Eulerian grids inside the particle boundaries are not used, thus Eq. (23) does not hold exactly; there should exist a term caused by the presence of the particles (we may refer to it as the direct effect of the particles). It is challenging to accurately compute the mean secondary flow [evidenced by the differences in three DNS results in Fig. 2(b)] and particularly the second-order derivatives of the Reynolds stresses, and the sum of four terms calculated is not exactly zero due to the computational error in the single-phase flow, as shown in Fig. 8(e). In Fig. 8(f), the computed sum of four terms for the particle-laden flow becomes larger, and it should contain both contributions from the particle direct effect and the computational error.

The contours of the mean streamwise vorticity computed from the mean secondary velocity field for the particle-free flow and the particle-laden flow at $a/H = 0.1$ and $\phi = 7.07\%$ are plotted in Figs. 6(a) and 6(b), respectively. The results show that the particles enhance the mean vorticity for most parts of the domain, particularly near the corner and the centerlines of the cross section. The enhancement in the mean vorticity is consistent with the enhancement in the stream-function observed earlier.

The spatial distributions of the last three terms in the mean vorticity equation (23) in a quadrant of the cross section for the particle-free flow and the particle-laden flow at $a/H = 0.1$ and $\phi = 7.07\%$ are compared in Fig. 7. The distribution of the convection term is not shown here, for convenience of the presentation of the figure, and considering that the magnitude of this term is much smaller than those of the other three terms. From Fig. 7, all three terms are generally enhanced by the addition of the particles, particularly near the corner. Since the terms involving the derivative of the Reynolds stresses are the source of the mean streamwise vorticity, their enhancements are responsible for the increase in the intensity of the mean secondary flow laden with large particles. We will discuss the effect of the particle direct effect later.

A more direct comparison of the terms involved in the vorticity equation (23) for the particle-free and particle-laden flows is made in Fig. 8, which shows the variations of the four terms along a line parallel to the y-axis at $z = -0.75$ terminating on the corner bisector. The particle-induced enhancements in the magnitudes of all terms are apparent. The viscous diffusion effect is much larger than the convection effect, as observed by Gavrilakis.[6] The vorticity diffusion serves as the balance term for the source terms involving the Reynolds stresses, and its pronounced negative values near the wall (around $y < -0.94$

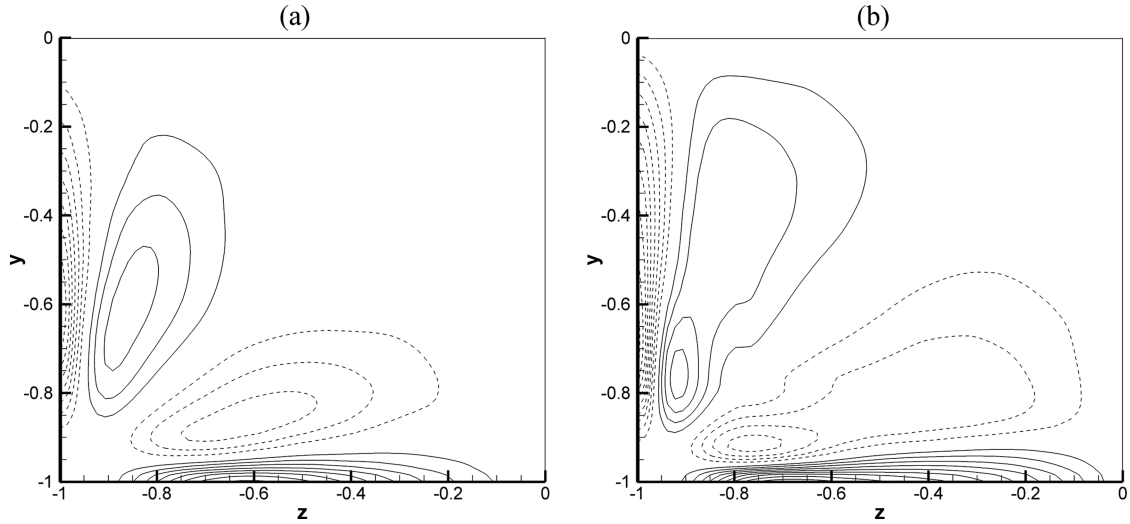

FIG. 6. Contours of the mean streamwise vorticity in a quadrant for (a) particle-free case and (b) $a/H = 0.1$ and $\phi = 7.07\%$. The increment for the contours is 1. Dashed lines correspond to negative values and solid lines to positive ones.

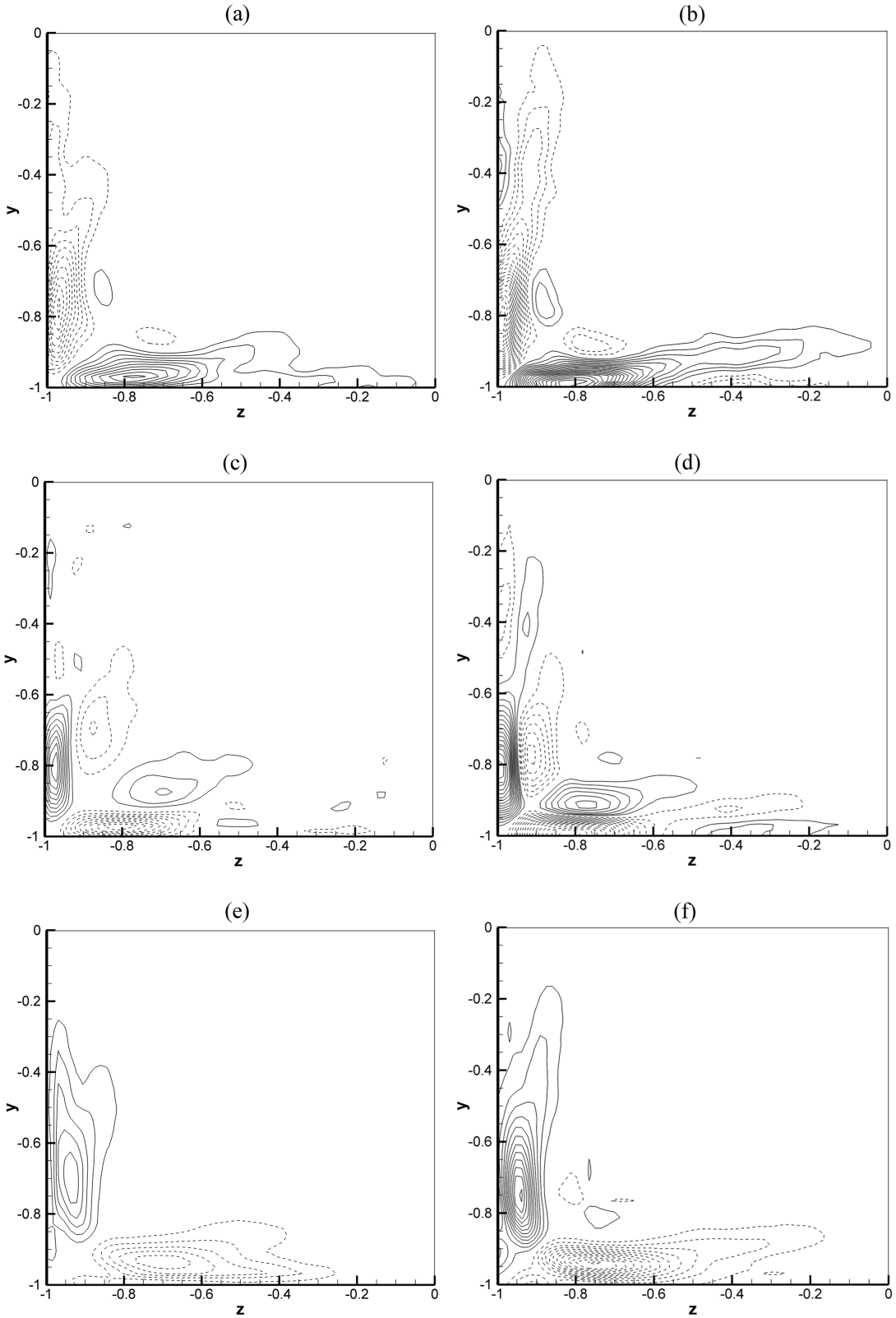

FIG. 7. The distributions of the three important terms in the mean vorticity equation for the [(a), (c), and (e)] particle-free flow and [(b), (d), and (f)] particle-laden flow at $a/H = 0.1$ and $\phi = 7.07\%$. Normal stress term: (a) and (b); shear stress term: (c) and (d); viscous diffusion term: (e) and (f). Dashed lines correspond to negative values and solid lines to positive ones. The increment for all contours is 3.

for the particle-laden case and $y < -0.91$ for the particle-free case) are mainly resulted from the considerable positive values of the normal stress difference term, whereas the Reynolds shear stress term contributes partly to the negative values of the viscous diffusion term for $-0.94 < y < -0.87$ in the case of particle-laden flow. Therefore, one may conclude that the particles enhance the mean secondary flow mainly through enhancing the gradients of the secondary Reynolds stresses

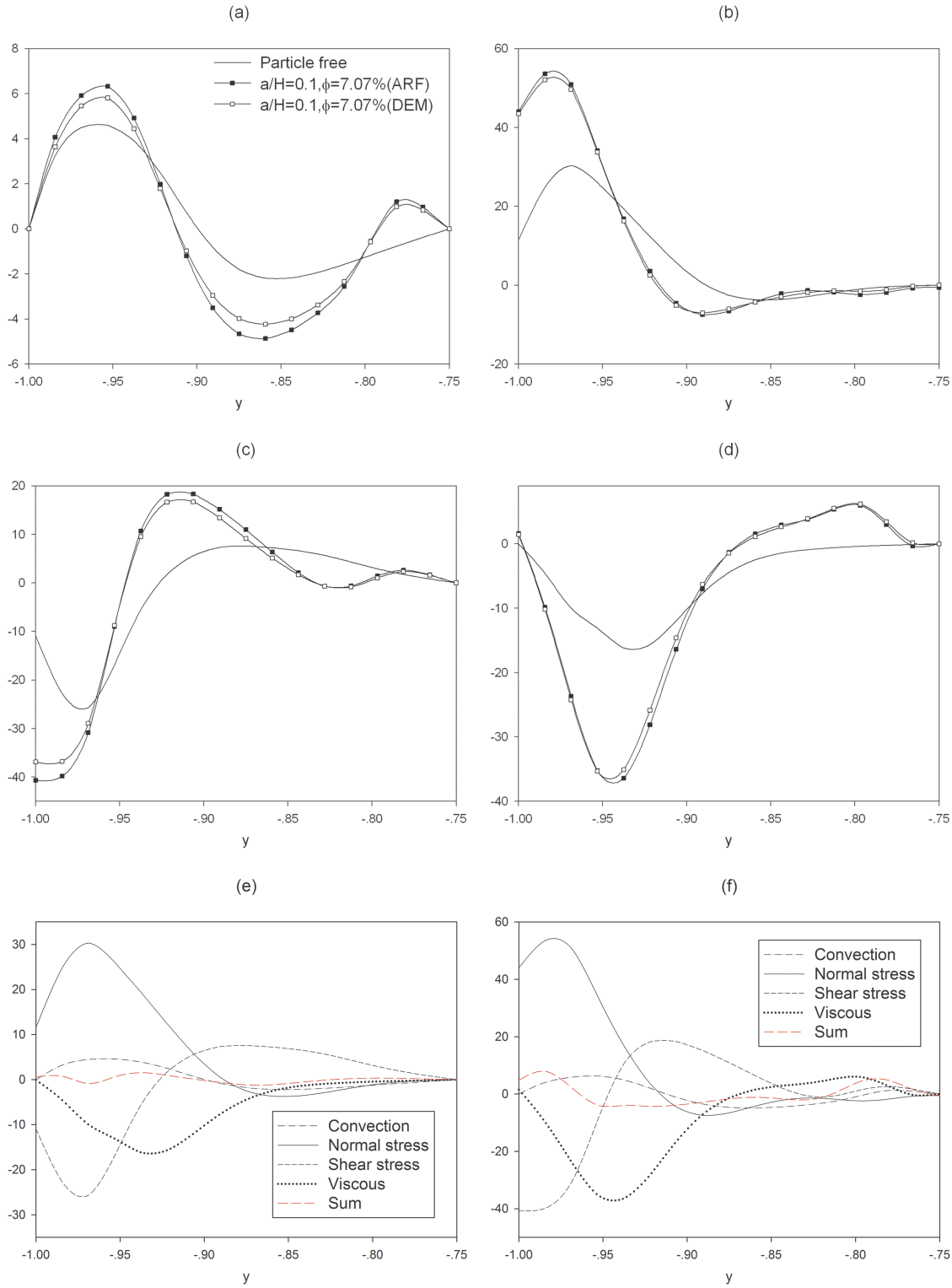

FIG. 8. The variations of the four terms in the mean vorticity equation along a line parallel to the y-axis at $z = -0.75$ terminating on the corner bisector for the particle-free and particle-laden cases. (a) convection term; (b) normal stress term; (c) shear stress term; (d) viscous diffusion term; (e) four terms and their sum for the particle-free case; (f) four terms and their sum for the particle-laden case with ARF.

(including both normal stress difference and shear stress) near the wall in the duct corner region. In addition, Fig. 8 shows that all terms in Eq. (23) for the DEM collision model are slightly smaller than those for the ARF model, consistent with the earlier observation in Fig. 5 that the mean secondary flow with the DEM model is weaker.

All four terms in Eq. (23) and their sum for the particle-free and particle-laden cases are plotted in Figs. 8(e) and 8(f), respectively. We have discussed earlier about the reasons why the sums are not zero for both cases, and as mentioned earlier, the computed sum for the particle-laden flow contains both contributions from the particle direct effect and the

computational error. The direct effect of the particles can also be the source of the mean secondary flow but since the computed sum is much smaller than the Reynolds stress terms (Fig. 8), we believe that the particle-induced enhancement in the gradients of the Reynolds stresses is responsible for the increase in the intensity of the mean secondary flow laden with large particles.

B. Mean streamwise velocity

The distributions of the mean streamwise velocity along the centerline at $z = 0$ for all cases are shown in Fig. 9(a). The velocities are reduced by the particle addition, and there is more reduction as the particle volume fraction increases at the same particle size or the particle size decreases at the same volume fraction. The bulk velocities calculated from the averaging the streamwise velocities over the whole cross section are presented in Fig. 9(b). We observe that the bulk velocities also decrease with increasing particle volume fraction or decreasing particle size. Since the mean pressure gradient is fixed, the reduction in the bulk velocity implies the enhancement in the flow drag. For the square duct flow, the friction factor can be defined as $f = 8u_\tau^2/U_b^2$.[39] The drag-enhancement by the finite-size particles was previously observed by Shao *et al.*[24] and Picano *et al.*[27] in the simulations of the plane turbulent channel flows. The more significant effect of smaller particles at the same volume fraction indicates that the effect caused by the particle number difference is more significant than the direct effect by the particle size.[24] For the case of $a/H = 0.05$ and $\phi = 7.07\%$, the bulk velocity is 12.65 for the DEM collision model and is 12.70 for the ARF model. The relative difference is around 0.4%, which may indicate that the contribution of the friction force exerted on the walls by the particles to the total drag (or wall shear force) is not important for the neutrally buoyant particles at the particle volume fraction up to 7.07%. For the ARF model, there is no direct friction force between the wall and the particles, but the particles slipping on the wall can increase the wall shear force by increasing the fluid shear rate at the wall (or in the gap between the particles and the wall). Nevertheless, for the case of heavy particles, the relative difference between the bulk velocities from two collision models can reach a few percent when most particles settle down to the bottom wall.[32]

C. RMS velocity

In this sub-section, we are concerned with the effects of the particles on the root-mean-square (RMS) values of the velocity fluctuations. The spatial distributions (contours) of the streamwise and spanwise RMS velocity components in the cross section are shown in Fig. 10. Both streamwise and spanwise RMS velocities first increase and then decrease as the distance away from the wall increases along the centerline in each direction, as in the plane channel flow. In the near-wall region, the RMS velocities decrease as the position shifts from the centerline toward the sidewall along a line parallel to the wall nearby, indicating that the constraint of the sidewalls attenuates the turbulence. Thus, the corner region has relatively low turbulent intensities. The spanwise RMS velocity component w^+_{rms} near the sidewall ($z = \pm 1$) actually represents the wall-normal component and is obviously seen to be smaller than the local wall-tangential component, i.e., w^+_{rms} near the lower or upper wall ($y = \pm 1$). The wall-normal RMS velocity in the near-wall region does not change much along the wall-tangential direction, unlike the streamwise and wall-tangential components.

Comparison between Figs. 10(a) and 10(b) shows that the streamwise RMS velocity is attenuated by the particles in most parts of the domain, except the regions close to the duct center and corners. By contrast, the spanwise RMS velocity w^+_{rms} is enhanced in the near-wall region, particularly in the near-corner region, as shown in Figs. 10(c) and 10(d). The increase in w^+_{rms} at $z = -0.75$ is more pronounced than that at $y = -0.75$ in the near-wall region, which means that $(w^2_{rms} - v^2_{rms})$ at $z = -0.75$ is enhanced by the particles, considering the symmetry that $v_{rms}(y, z) = w_{rms}(z, y)$ for the neutrally buoyant case. We have observed earlier that the particles enhance the gradients of the normal stress difference near the corner, and we now show that this increase in the gradients of the normal stress difference is resulted from more increase in the wall-tangential component than the wall-normal component.

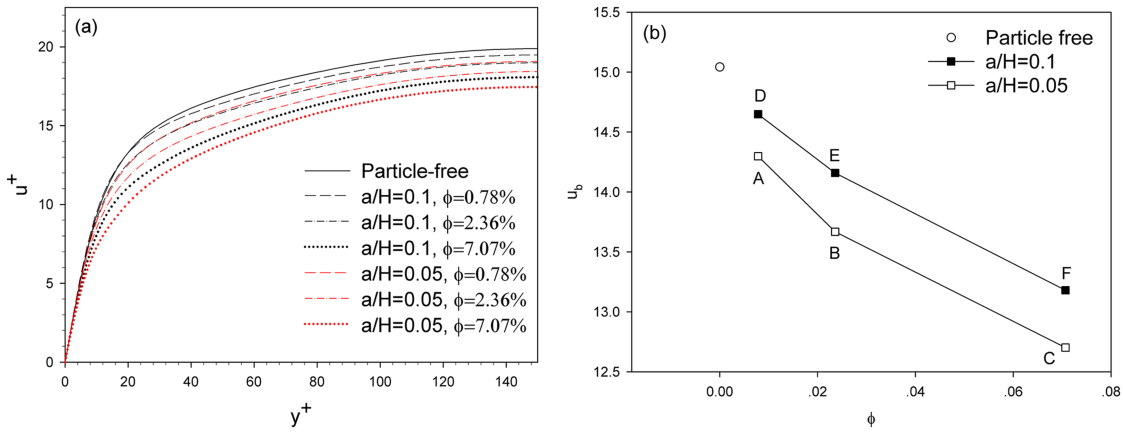

FIG. 9. (a) Mean streamwise velocity distribution along a line parallel to the y-axis: $z = 0$ and (b) the bulk velocity as a function of the particle volume fraction: Point "A": $a/H = 0.05$, $\phi = 0.78\%$; "B": $a/H = 0.05$, $\phi = 2.36\%$; "C": $a/H = 0.05$, $\phi = 7.07\%$; "D": $a/H = 0.1$, $\phi = 0.78\%$; "E": $a/H = 0.1$, $\phi = 2.36\%$; "F": $a/H = 0.1$, $\phi = 7.07\%$.

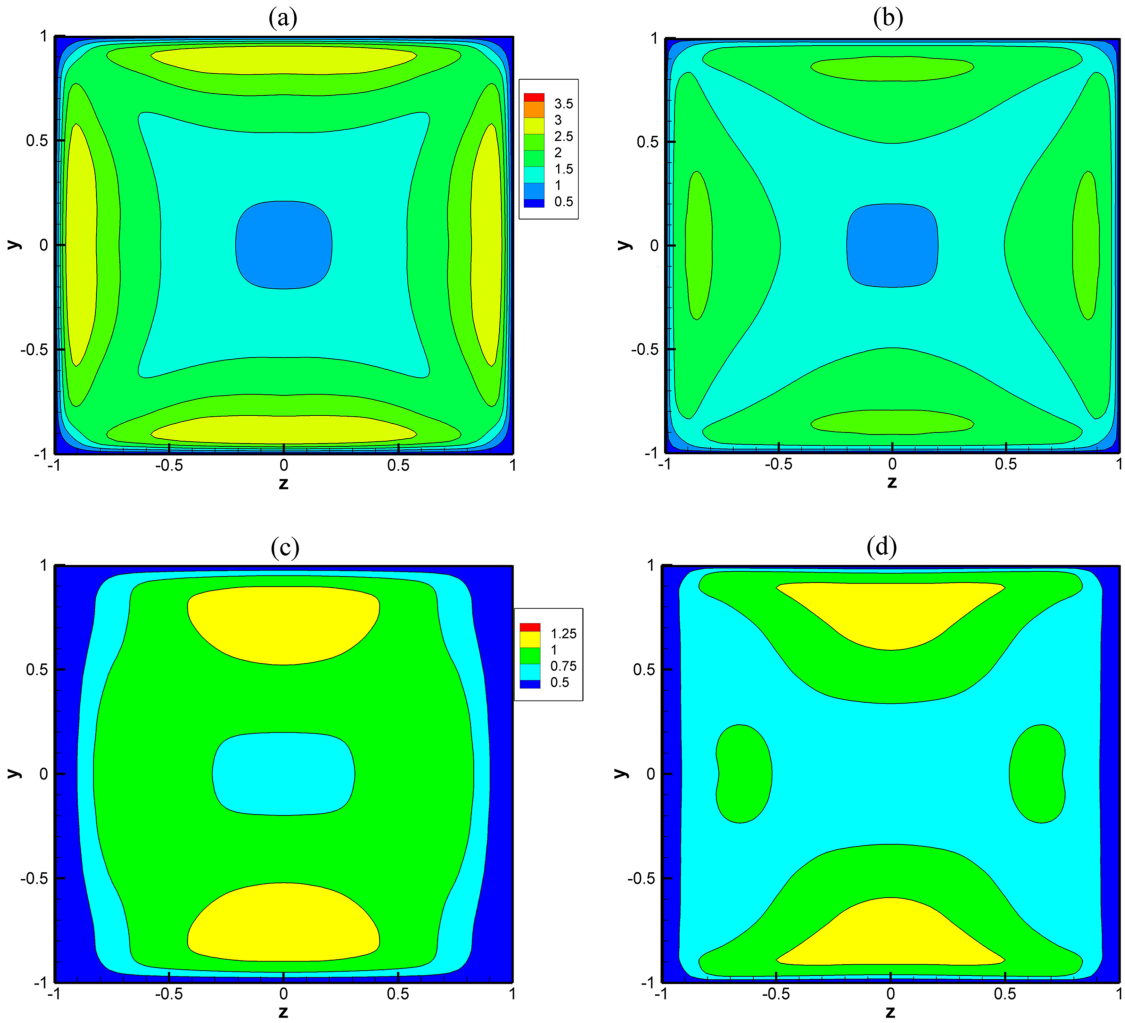

FIG. 10. The distributions of the root-mean-square values of the [(a) and (b)] streamwise and [(c) and (d)] spanwise velocity fluctuation components for [(a) and (c)] particle-free flow and [(b) and (d)] particle-laden flow at $a/H = 0.05$ and $\phi = 7.07\%$.

A more direct comparison of the RMS velocity components between the particle-free and particle-laden cases is presented in Fig. 11, which shows the RMS velocity profiles at $z = 0$ and $z = -0.5$ for the particle-free case and particle-laden cases with $a/H = 0.1$. The results support the above findings from Fig. 10. For example, the pronounced attenuation in the streamwise RMS velocity peak and enhancement in the cross-stream components near the wall at $z = -0.5$ can be observed in Fig. 11. Qualitatively same results were found by Shao *et al.*[24] in the plane channel flow, who attributed the reason for the attenuation in the streamwise RMS velocity peak to the weakening of the large-scale vortices caused by the particle-induced viscous dissipation and the disturbance (or competition) from the particle-induced vortices, and the reason for the enhancement in the cross-stream RMS velocities in the near-wall region to the effects of the particle-induced vortices. These explanations also apply to the duct flow studied here. The particle-induced vortices in the near-wall region are expected to cause the enhancement in the gradients of the secondary Reynolds stresses observed earlier. The vortex structures identified as the iso-surfaces of the imaginary part of the complex eigenvalue of the velocity gradient tensor (i.e., the λci criterion proposed by Zhou *et al.*[40]) for the single-phase flow and the particle-laden flow at $\phi = 7.07\%$ are compared in Fig. 12. The weakening of the large-scale vortices and the particle-induced smaller-scale vortices near the wall in the particle-laden flows can be observed. Similar weakening of large-scale vortex structures was observed in the channel particle-laden flows by Dritselis and Vlachos.[41]

The mean turbulent kinetic energies (TKEs) of the entire flow for all cases with the ARF model are plotted in Fig. 13. The TKE decrease with increasing particle volume fraction and decreasing particle size, if other parameters are fixed. This behavior of the TKE is same as that of the bulk velocity in Fig. 9(b) or opposite to that of the flow drag. The reduction in the TKE means the suppression of the turbulence (e.g., Reynolds shear stress), and thus corresponds to the drag-reduction for the single-phase turbulence, whereas for the particle-laden turbulence studied, it corresponds to the drag-enhancement, indicating that the drag-enhancement in the particle-laden flow is caused by the particle-fluid interphase drag force or the particle stress. Results of point-particle direct numerical simulations of downward gas–solid flows

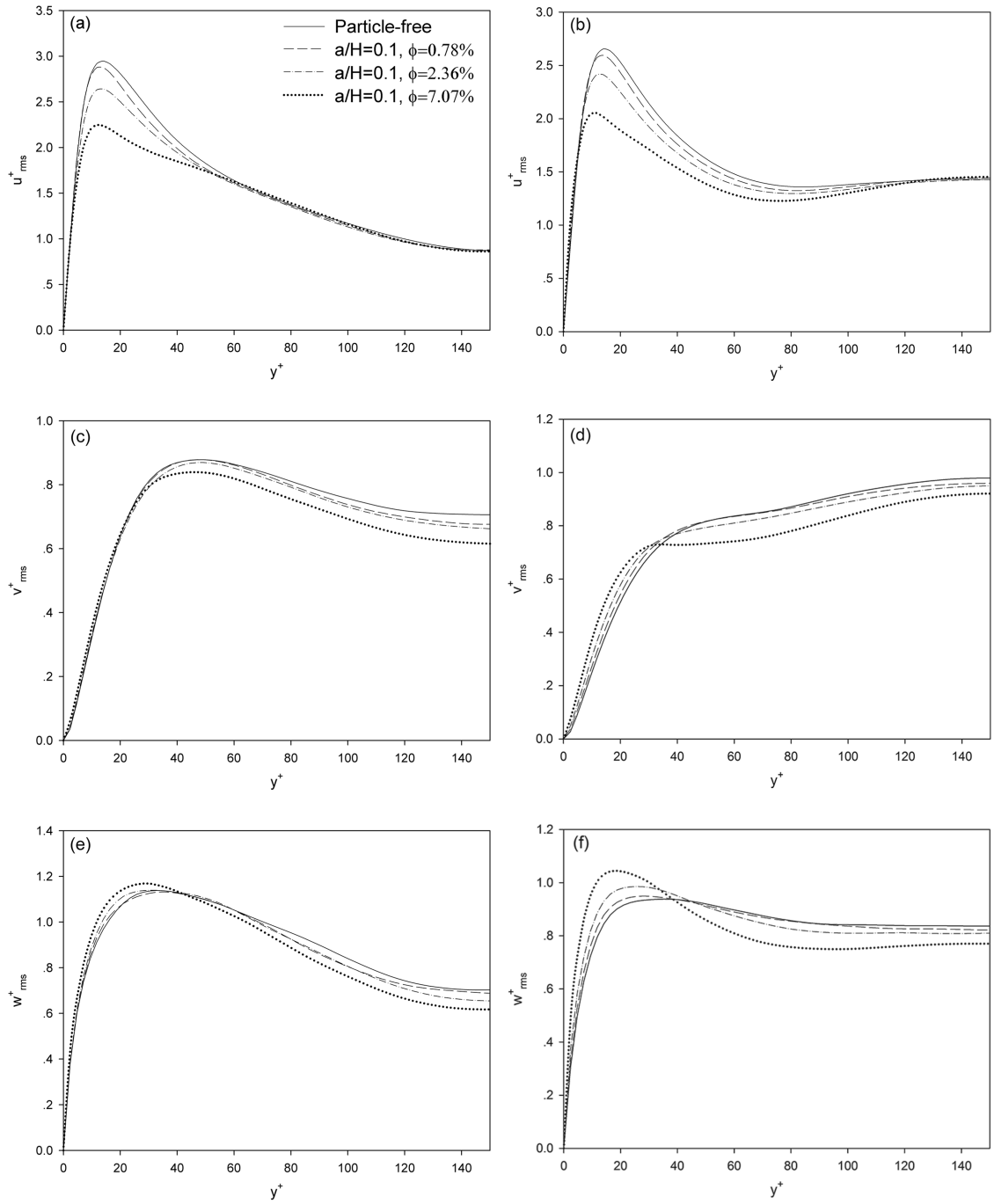

FIG. 11. The profiles of the root-mean-square of the [(a) and (b)] streamwise, [(c) and (d)] transverse, and [(e) and (f)] spanwise velocity fluctuations along a line parallel to the y-axis at [(a), (c), and (e)] $z = 0$ and [(b), (d), and (f)] $z = -0.5$ for the particle-free and particle-laden turbulent duct flows.

in pipe and channel flows showed that non-uniformity of the mean drag loading could account for a large part of the turbulence attenuation.[42,43] It would be an interesting subject of future study to examine the possible effect of non-uniformity of mean drag on the turbulence attenuation in duct flows.

D. Solid-phase statistics

The solid-phase statistic that we are mainly concerned with in the present study is the spatial distribution of the particle concentration in the cross section. Its value at (y_j, z_k) is approximated as the probability of this cross-stream position covered by the particles,

$$\xi(y_j, z_k) = \frac{\sum\limits_{x_i,t} i_s(x_i, y_j, z_k, t)}{N(y_j, z_k)}, \tag{24}$$

where $i_s(x_i, y_j, z_k, t)$ equals 1 if the grid (x_i, y_j, z_k) is found to be located in the particle domain and zero otherwise, and $N(y_j, z_k)$ is the total check number of the grid (y_j, z_k) for different x_i and t.

Figure 14 shows that the particles accumulate in the corner region. For the wall-bounded turbulent flows, a rise in the

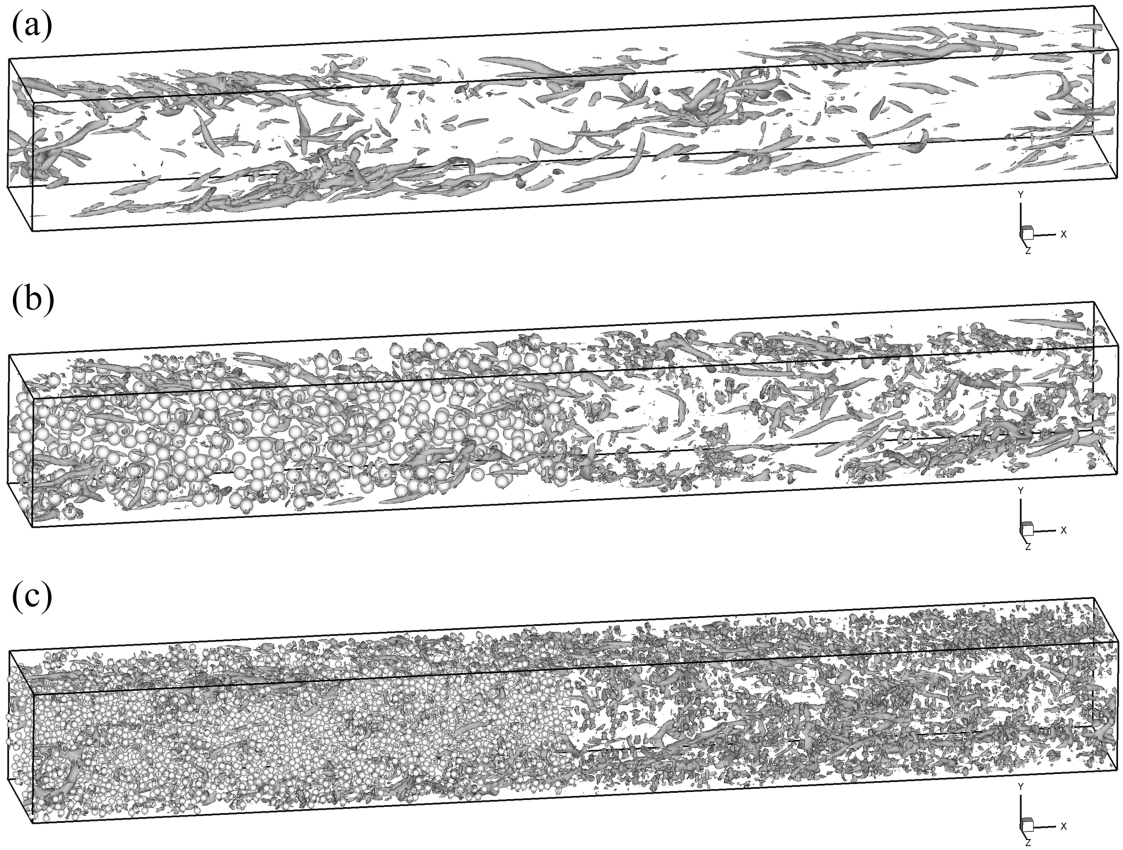

FIG. 12. Vortex structures for (a) particle-free case; (b) $a/H = 0.1$, $\phi = 7.07\%$ (with DEM); (c) $a/H = 0.05$, $\phi = 7.07\%$ (with DEM). The particles are shown only in the half duct for the clarity of the vortex structures.

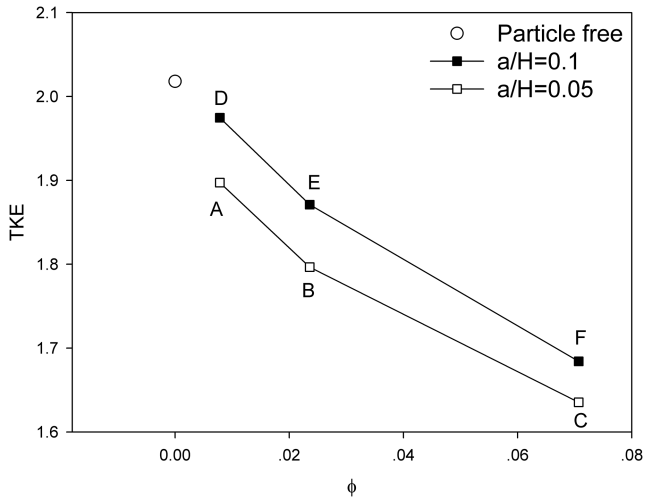

FIG. 13. Turbulent kinetic energy as a function of the particle volume fraction. Point "A": $a/H = 0.05$, $\phi = 0.78\%$; "B": $a/H = 0.05$, $\phi = 2.36\%$; "C": $a/H = 0.05$, $\phi = 7.07\%$; "D": $a/H = 0.1$, $\phi = 0.78\%$; "E": $a/H = 0.1$, $\phi = 2.36\%$; "F": $a/H = 0.1$, $\phi = 7.07\%$.

particle volume fraction near the wall was commonly observed (e.g., Reeks,[44] Young and Leeming,[45] and Uhlmann[21]). The main mechanism for this particle preferential accumulation was recognized as turbophoresis, an average migration of particles in the direction opposite to gradients in the turbulence intensity (specifically the wall-normal RMS velocity). For an individual particle, this means that it is less probable to receive the necessary momentum driving it from a region of low turbulence intensity toward a high intensity region than vice versa.[21] Such turbophoresis effect takes place only for the particles with the density larger than that of the carrier fluid. If one considers particles lighter than the fluid, or bubbles, the effect will be the opposite: particles or bubbles will migrate from regions of low turbulence intensity to the regions of high turbulence intensity, as pointed out by an anonymous referee of the present paper. Therefore, for the present case of neutrally buoyant particles, the turbophoresis effect cannot be used to explain the preferential concentration of the particles in the corner region. Then, the mean secondary flow is the most probable reason for this preferential concentration of the particles, which drives the particles toward the corner region and away from the wall at the wall bisector in a statistical sense. In the case of $\phi = 2.36\%$, the particle concentrations at the regions close to the corner and the wall center are lower than the average concentration [Fig. 14(a)], and the reason may be related to the fact that these two positions are the stagnation points of the mean secondary flow [Fig. 4(a)] and the mean secondary flow does not drive the particles toward the stagnation point. By contrast, for $\phi = 7.07\%$, the particle concentration at the corner is considerably high, and our explanation is that the particle interactions (such as collision) at a relatively high particle volume can increase significantly the probability of the particles entering this corner region and the particles could be trapped there for a relatively long time once entering.

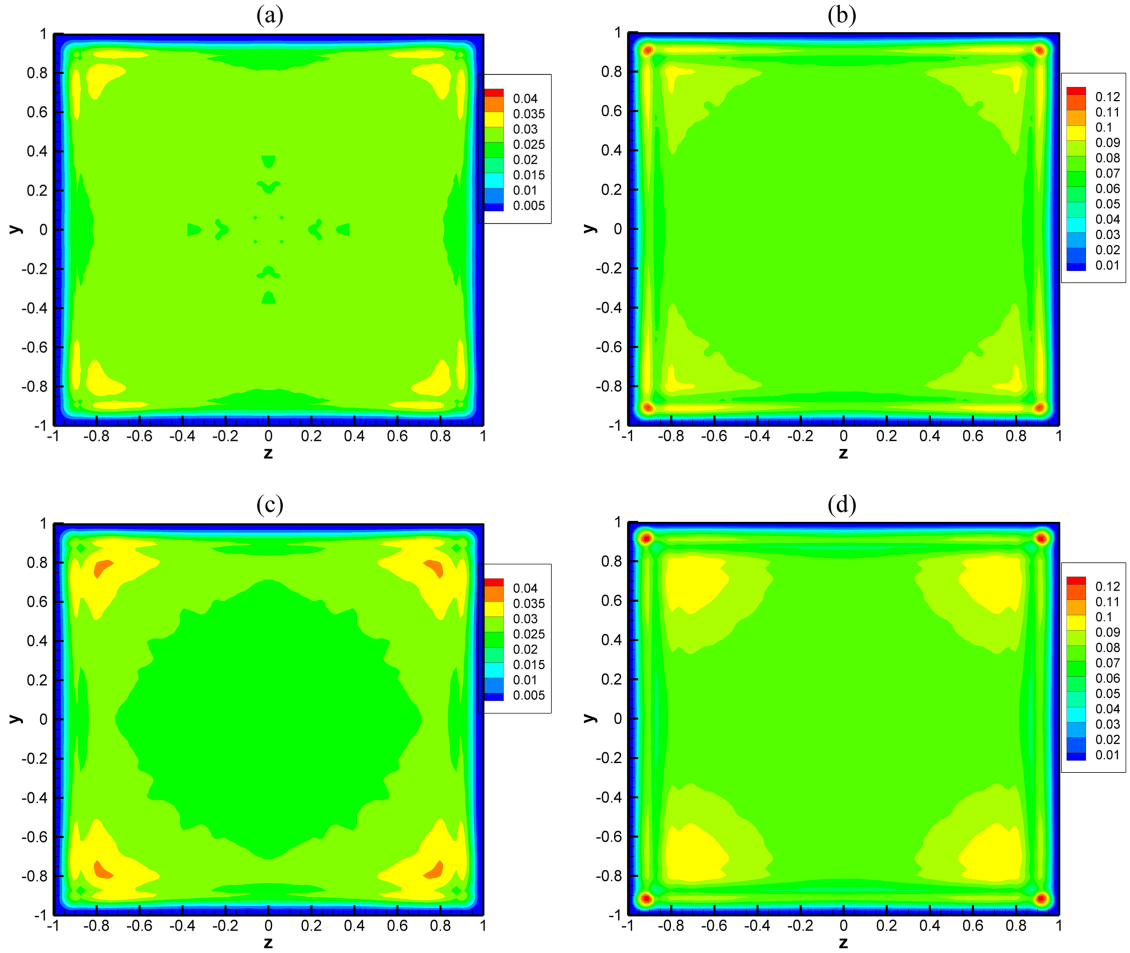

FIG. 14. The spatial distributions of the local particle volume fraction in the cross section: (a) $a/H = 0.05$, $\phi = 2.36\%$, with ARF; (b) $a/H = 0.05$, $\phi = 7.07\%$, with ARF; (c) $a/H = 0.05$, $\phi = 2.36\%$, with DEM; (d) $a/H = 0.05$, $\phi = 7.07\%$, with DEM.

There is a gap of low particle concentrations separating the region of high particle concentrations in each direction for $\phi = 7.07\%$, as shown in Fig. 14. This phenomenon was previously observed in the planar channel flow (Uhlmann,[21] Picano,[26] and Wang *et al.*[27]); Uhlmann[21] conjectured that it was still the result of the turbophoresis effect, whereas Wang *et al.*[27] argued that it was caused by the lift force. Because this gap is located around one particle diameter away from the wall, the reason might be related to the blocking (volume-excluding) effect of the particles nearly touching the wall, which play a role as a wall, causing a region of low particle volume fractions observed. The observation that this gap of low particle concentrations is much more pronounced for $\phi = 7.07\%$ than for $\phi = 2.36\%$ in Fig. 14 may indicate that the particle interaction plays an important role in its formation. To show a more direct evidence for this conjecture, the spatial distribution of the average collision force on the particles in the y-direction for $a/H = 0.05$ and $\phi = 7.07\%$ with the ARF collision model is plotted in Fig. 15(c). The force is assumed to be located at the particle center. In Fig. 15(c), there are three force bands, extended in the z-direction. The forces in the upper band are positive (i.e., pointing upwards) and most pronounced. Since the upper band is located at around $y = -0.85$, namely 3 particle radii away from the bottom wall, it is reasonable to attribute this force band to the collision of the particles in this band with those particles nearly touching the bottom wall. The most conspicuous collision force patch in this band near the corner at $z = -0.9 \sim 085$ is expected to be mainly caused by the collision of the particles there with the particles trapped in the corner at $\phi = 7.07\%$. The other two thinner bands below the main band in Fig. 15(c) are clearly sourced from the collision forces on the particles nearly touching the bottom wall. These forces are weaker because they are net forces and the collision forces on these particles from the wall and the upper particles counteract with each other in the statistical sense (the two forces may act on the particles at the same time or at the different times). The probable reason for the positive forces in the lowest band and the negative forces in the middle band is that the repulsive collision forces from the wall prevail when the particles are closer to the wall and the collision forces from the upper particles prevail when the particles move farther away the wall.

Figure 15 also shows the y-component of the average hydrodynamic force on the particles with the ARF collision model and the collision and hydrodynamic forces with the DEM collision model. One can observe that the distribution of the average hydrodynamic force is closely correlated to that of the collision force, indicating that the hydrodynamic force in the near-wall region is significantly affected (or mainly caused) by the particle collision which gives rise to the rapid

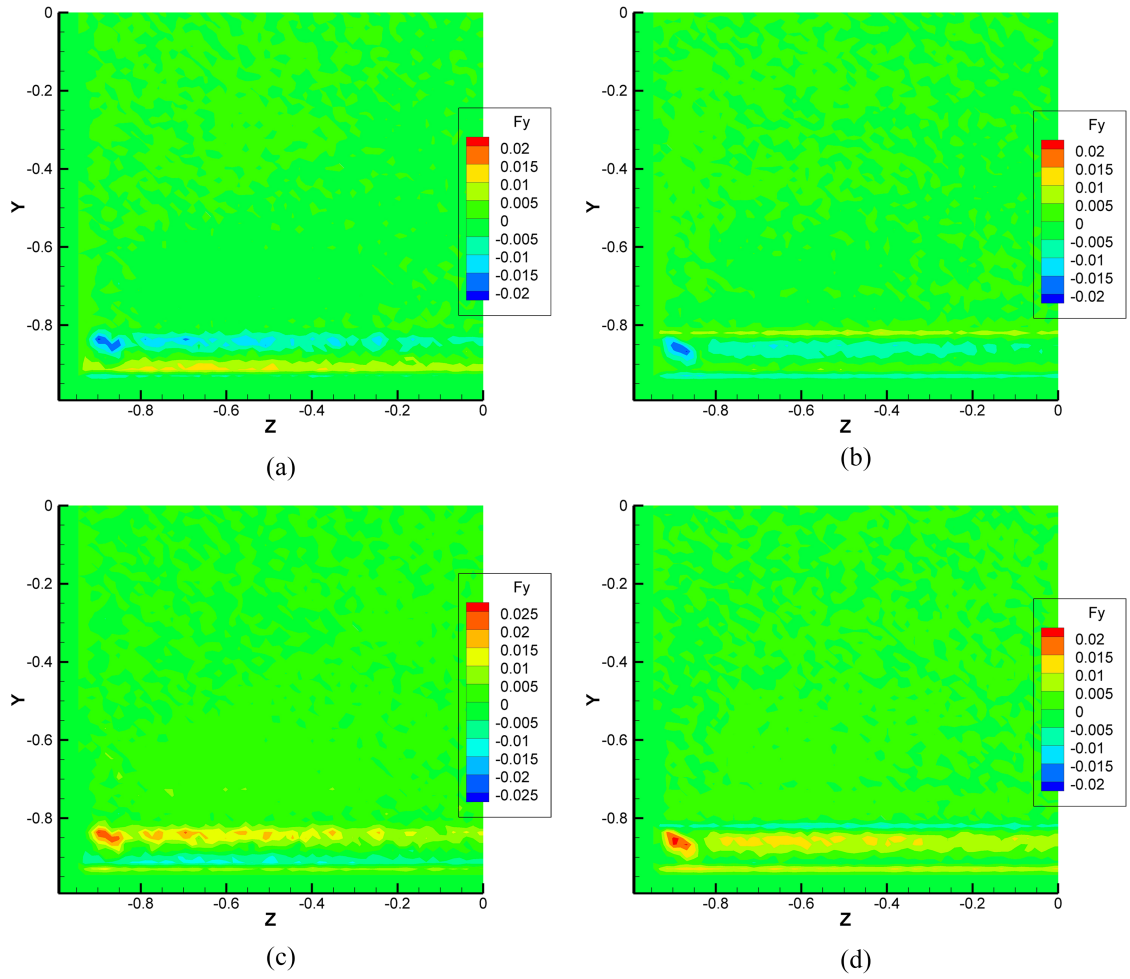

FIG. 15. The spatial distributions of the average [(a) and (b)] hydrodynamic force and [(c) and (d)] collision force on the particles in the y-direction at $a/H = 0.05$ and $\phi = 7.07\%$ with ARF for (a) and (c) and DEM for (b) and (d).

change in the particle velocity (and the slip velocity). For the DEM model, there also exists a primary band similar to that for the ARF model. There are differences in the other minor force bands for two collision models, which could be explained by the differences in two collision models such as the viscous damping force in the DEM model which is repulsive in the approaching process and attractive in the separation process. How the collision model and parameters affect the particle motion and distributions is a subject of future study. In the present study, we mainly attempt to show that the collision model has important quantitative effects on the results but does not modify the results qualitatively.

The profiles of the solid-phase streamwise mean velocities at $z = 0$ and -0.5 and the distributions of the solid-phase streamwise and spanwise RMS velocity components for $a/H = 0.05$ and $\phi = 7.07\%$ are plotted in Figs. 16 and 17, respectively. In the bulk region, the solid-phase streamwise mean velocity is roughly the same as the fluid-phase mean velocity, in the region very close to the wall, the solid-phase velocity is considerably larger than the fluid-phase velocity, and in the region of $y \approx -0.9$ (around one particle diameter away from the wall), the solid-phase velocity is smaller than the fluid-phase velocity. These observations are in qualitatively agreement with the previous interphase-resolved DNS results

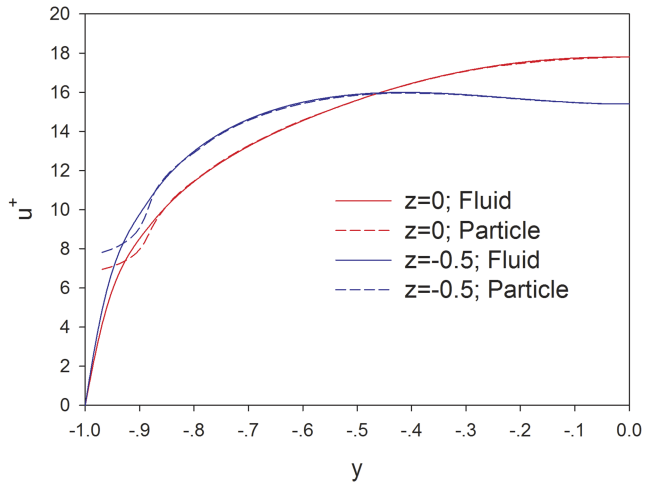

FIG. 16. The profiles of the solid-phase streamwise mean velocities at $z = 0$ and -0.5 for $a/H = 0.05$ and $\phi = 7.07\%$.

on the turbulent channel flows.[27,28] The comparison between Figs. 10 and 17 shows that the particle RMS velocities are smaller than the fluid counterparts, which is also consistent with the results on the turbulent channel flow laden with the neutrally buoyant particles.[27]

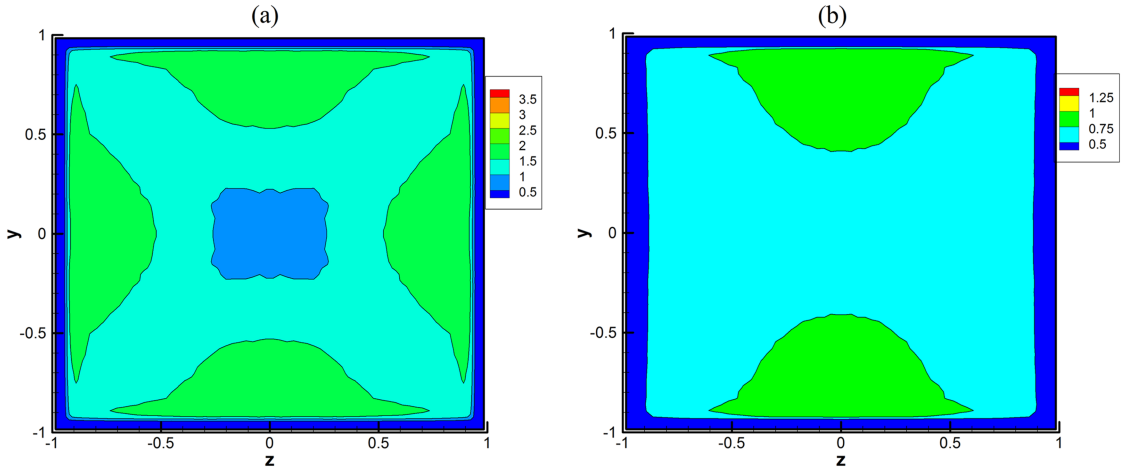

FIG. 17. The distributions of the root-mean-square values of the solid-phase (a) streamwise and (b) spanwise velocity fluctuation components for $a/H = 0.05$ and $\phi = 7.07\%$.

V. CONCLUSIONS

We have performed the interface-resolved direct numerical simulations of the particle-laden turbulent flows in a square duct with a direct-forcing fictitious domain method. The effects of the finite-size neutrally buoyant particles ($a/H = 0.05$ and 0.1) on the mean and root-mean-square (RMS) velocities and the distribution of the particle volume fraction have been investigated at $Re_\tau = 150$ and $\phi = 0.78\%$–7.07%. There are two main findings from our studies that are specific to the square duct geometry. The primary one is that the particle addition enhances the mean secondary flow and makes its circulation center shift closer to the center of the duct cross section. The main mechanism for the enhancement in the mean secondary flow is that the particles enhance the gradients of the secondary Reynolds normal stress difference and the Reynolds shear stress, by inducing the vortex structures near the wall. The other new finding is that the particles accumulate preferentially in the near-corner region, which is presumably caused by the mean secondary flow effect. The particle distribution is affected by the particle-particle and particle-wall collision model used, and the blocking effects of the particles nearly touching the wall are responsible for the band of low solid volume fraction located around one particle diameter away from the wall.

Furthermore, results similar to the particle-laden planar channel flow are found, concerning the effects of solid particles on the mean streamwise flow velocity and turbulence intensity away from the duct corner regions: under a prescribed mean driving pressure gradient, the mean streamwise flow speed is reduced, the wall friction is increased, turbulent kinetic energy is attenuated, streamwise rms velocity is attenuated but the spanwise rms velocity is augmented near a wall. These effects increase with increasing particle volume fraction or decreasing particle size.

ACKNOWLEDGMENTS

The work was supported by the National Natural Science Foundation of China (Grant Nos. 11372275 and 11632016), and Research Fund for the Doctoral Program of Higher Education of China (No. 20130101110035). L.P.W. is supported by the U.S. National Science Foundation (NSF) under No. CBET-1235974 and by the Air Force Office of Scientific Research under No. FA9550-13-1-0213. Computing resources at Yellowstone supercomputer are provided by the National Center for Atmospheric Research through Nos. CISL-P35751014 and CISL-UDEL0001 and by the University of Delaware through NSF No. CRI 0958512.

[1]L. Prandtl, "Über die ausgebildete turbulenz," Ver. 2nd Int. Kongr. Tech. Mech., Zurich (1926) [NACA Tech. Memo. **435**, 62 (1926)].
[2]J. Nikuradse, "Untersuchungen über die geschwindigkeitsverteilung in turbulenten ctrömungen," Ph.D. thesis, VDI Forsch. 281, Göttingen, 1926.
[3]E. Brundrett and W. Baines, "The production and diffusion of vorticity in duct flow," J. Fluid Mech. **19**, 375–394 (1964).
[4]F. Gessner, "The origin of secondary flow in turbulent flow along a corner," J. Fluid Mech. **58**, 1–25 (1973).
[5]A. Melling and J. Whitelaw, "Turbulent flow in a rectangular duct," J. Fluid Mech. **78**, 289–315 (1976).
[6]S. Gavrilakis, "Numerical simulation of low-Reynolds-number turbulent flow through a straight square duct," J. Fluid Mech. **244**, 101–129 (1992).
[7]A. Huser and S. Biringen, "Direct numerical simulation of turbulent flow in a square duct," J. Fluid Mech. **257**, 65–95 (1993).
[8]M. Uhlmann, A. Pinelli, G. Kawahara, and A. Sekimoto, "Marginally turbulent flow in a square duct," J. Fluid Mech. **588**, 153–162 (2007).
[9]A. Pinelli, M. Uhlmann, A. Sekimoto, and G. Kawahara, "Reynolds number dependence of mean flow structure in square duct turbulence," J. Fluid Mech. **644**, 107–122 (2010).
[10]C. M. Winkler, S. L. Rani, and S. P. Vanka, "Preferential concentration of particles in a fully developed turbulent square duct flow," Int. J. Multiphase Flow **30**, 27–50 (2004).
[11]G. Sharma and D. J. Phares, "Turbulent transport of particles in a straight square duct," Int. J. Multiphase Flow **32**, 823–837 (2006).
[12]C. M. Winkler, S. L. Rani, and S. P. Vanka, "A numerical study of particle wall-deposition in a turbulent square duct flow," Powder Technol. **170**, 12–25 (2006).
[13]J. Yao and M. Fairweather, "Particle deposition in turbulent duct flows," Chem. Eng. Sci. **84**, 781–800 (2012).
[14]J. Yao, M. Fairweather, and Y. L. Zhao, "Numerical simulation of particle deposition in turbulent duct flows," Ind. Eng. Chem. Res. **53**, 3329–3341 (2014).
[15]J. Yao and M. Fairweather, "Inertial particle resuspension in a turbulent square duct flow," Phys. Fluids **22**, 033303 (2010).
[16]A. Ten Cate, J. J. Derksen, L. M. Portela, and H. E. A. van den Akker, "Fully resolved simulations of colliding monodisperse spheres in forced isotropic turbulence," J. Fluid Mech. **519**, 233–271 (2004).

[17]F. Lucci, A. Ferrante, and S. Elghobashi, "Modulation of isotropic turbulence by particles of Taylor length-scale size," J. Fluid Mech. **650**, 5–55 (2010).
[18]H. Gao, H. Li, and L.-P. Wang, "Lattice Boltzmann simulation of turbulent flow laden with finite-size particles," Comput. Math. Appl. **65**, 194–210 (2013).
[19]M. Cisse, H. Homann, and J. Bec, "Slipping motion of large neutrally buoyant particles in turbulence," J. Fluid Mech. **735**, R1 (2013).
[20]T. Wu, X. Shao, and Z. Yu, "Fully resolved numerical simulation of turbulent pipe flows laden with large neutrally-buoyant particles," J. Hydrodyn., Ser. B **23**, 21–25 (2011).
[21]M. Uhlmann, "Interface-resolved direct numerical simulation of vertical particulate channel flow in the turbulent regime," Phys. Fluids **20**, 053305 (2008).
[22]M. García-Villalba, A. G. Kidanemariam, and M. Uhlmann, "DNS of vertical plane channel flow with finite-size particles: Voronoi analysis, acceleration statistics and particle-conditioned averaging," Int. J. Multiphase Flow **46**, 54–74 (2012).
[23]Y. Pan and S. Banerjee, "Numerical investigation of the effects of large particles on wall turbulence," Phys. Fluids **9**, 3786–3807 (1997).
[24]X. Shao, T. Wu, and Z. Yu, "Fully resolved numerical simulation of particle-laden turbulent flow in a horizontal channel at a low Reynolds number," J. Fluid Mech. **693**, 319–344 (2012).
[25]A. G. Kidanemariam, C. Chan-Braun, T. Doychev, and M. Uhlmann, "Direct numerical simulation of horizontal open channel flow with finite-size, heavy particles at low solid volume fraction," New J. Phys. **15**, 025031 (2013).
[26]M. Do-Quang, G. Amberg, G. Brethouwer, and A. V. Johansson, "Simulation of finite-size fibers in turbulent channel flows," Phys. Rev. E **89**, 013006 (2014).
[27]F. Picano, W.-P. Breugem, and L. Brandt, "Turbulent channel flow of dense suspensions of neutrally buoyant spheres," J. Fluid Mech. **764**, 463–487 (2015).
[28]L.-P. Wang, P. Gao, Z. Guo, and Z. Yu, "Flow modulation by finite-size neutrally buoyant particles in a turbulent channel flow," ASME J. Fluids Eng. **138**, 041306 (2016).
[29]P. Bagchi and S. Balachandar, "Effect of turbulence on the drag and lift of a particle," Phys. Fluids **15**, 3496–3513 (2003).
[30]T. M. Burton and J. K. Eaton, "Fully resolved simulations of particle-turbulence interaction," J. Fluid Mech. **545**, 67–111 (2005).
[31]A. Naso and A. Prosperetti, "The interaction between a solid particle and a turbulent flow," New J. Phys. **12**, 033040 (2010).
[32]Z. W. Lin, X. M. Shao, Z. S. Yu, and L.-P. Wang, "Effects of finite-size heavy particles on the turbulent flows in a square duct," J. Hydrodyn., Ser. B **29**, 272–282 (2017).
[33]Z. Yu, Z. Lin, X. Shao, and L.-P. Wang, "A parallel fictitious domain method for the interface-resolved simulation of particle-laden flows and its application to the turbulent channel flow," Eng. Appl. Comput. Fluid Mech. **10**, 160–170 (2016).
[34]R. Glowinski, T. W. Pan, T. I. Hesla, and D. D. Joseph, "A distributed Lagrange multiplier/fictitious domain method for particulate flows," Int. J. Multiphase Flow **25**, 755–794 (1999).
[35]Z. Yu and X. Shao, "A direct-forcing fictitious domain method for particulate flows," J. Comput. Phys. **227**, 292–314 (2007).
[36]C. T. Crowe, J. D. Schwarzkopf, M. Sommerfeld, and Y. Tsuji, *Multiphase Flows With Droplets and Particles* (CRC Press, Florida, USA, 2011).
[37]T. Kempe and J. Fröhlich, "Collision modelling for the interface-resolved simulation of spherical particles in viscous fluids," J. Fluid Mech. **709**, 445–489 (2012).
[38]J. Perkins, "The formation of streamwise vorticity in turbulent flow," J. Fluid Mech. **44**, 721–740 (1970).
[39]O. Jones, "An improvement in the calculation of turbulent friction in rectangular ducts," ASME J. Fluids Eng. **98**, 173–181 (1976).
[40]J. Zhou, R. J. Adrian, S. Balachandar, and T. M. Kendall, "Mechanisms for generating coherent packets of hairpin vortices in channel flow," J. Fluid Mech. **387**, 353–396 (1999).
[41]C. D. Dritselis and N. S. Vlachos, "Numerical investigation of momentum exchange between particles and coherent structures in low Re turbulent channel flow," Phys. Fluids **23**, 025103 (2011).
[42]A. W. Vreman, "Turbulence characteristics of particle-laden pipe flow," J. Fluid Mech. **584**, 235–279 (2007).
[43]A. W. Vreman, "Turbulence attenuation in particle-laden flow in smooth and rough channels," J. Fluid Mech. **773**, 103–136 (2015).
[44]M. W. Reeks, "The transport of discrete particles in inhomogeneous turbulence," J. Aerosol Sci. **14**, 729–739 (1983).
[45]J. Young and A. Leeming, "A theory of particle deposition in turbulent pipe flow," J. Fluid Mech. **340**, 129–159 (1997).